Energy & Environmental Science

Accepted Manuscript

ROYAL SOCIETY OF CHEMISTRY

www.rsc.org/ees

Dramatically enhanced reversibility of Li_2O in SnO_2-based electrodes: the effect of nanostructure on high initial reversible capacity

Renzong Hu,[a, b] Dongchang Chen,[b] Gordon Waller,[b] Yunpeng Ouyang,[a] Yu Chen,[b] Bote Zhao,[b] Ben Rainwater,[b] Chenghao Yang,[c] Min Zhu,*[a] Meilin Liu*[b, c]

[a] School of Materials Science and Engineering, South China University of Technology, Guangzhou, 510640, China. E-mail: memzhu@scut.edu.cn

[b] School of Materials Science and Engineering, Georgia Institute of Technology, Atlanta, GA 30332-0245, USA.E-mail: meilin.liu@mse.gatech.edu

[c] School of Environment and Energy, South China University of Technology, Guangzhou, 510006, China

Abstract:

The formation of irreversible Li_2O during discharge is believed to be the main cause of large capacity loss and low Coulombic efficiency of oxide negative electrodes for Li batteries. This assumption may have misguided the development of high-capacity SnO_2-based anodes in recent years. Here we demonstrated that contrary to this perception, Li_2O can indeed be highly reversible in a SnO_2 electrode with controlled nanostructure and achieved an initial Coulombic efficiency of ~95.5%, much higher than that previously believed possible (52.4%). *Insitu* spectroscopic and diffraction analyses corroborate the highly reversible electrochemical cycling, suggesting that the interfaces and grain boundaries of nano-sized SnO_2 may suppress the coarsening of Sn and enable the conversion between Li_2O and Sn to amorphous SnO_2 when de-lithiated. These results provide important insight into the rational design of high-performance oxide electrodes for Li-ion batteries.

Board context

Further advances in Li-ion battery technology depend critically on the creation of novel electrode materials or the new architecture design for the high capacity electrodes. Tin dioxide (SnO_2) has been considered one of the most promising alternative anode materials for lithium batteries. In the past two decades, extensive studies have been directed to gaining a fundamental understanding of the lithiation/delithiation reactions to improve the performance of SnO_2-based electrodes. However, the conversion reaction in lithiated SnO_2 that produces Li_2O has long been believed irreversible and considered the main cause of large capacity loss and low Coulombic efficiency of SnO_2 and other oxide electrodes. Accordingly, a key question highlighted in Chiang's *Perspectives* (Building a better Battery, *Science*, 2010, 330, 1485) is how to overcome the irreversibility of Li_2O in SnO_2 anode to fully exploiting the limit of the capacity of the electrode materials. This work demonstrates that suppressing the coarsening of *in situ* formed Sn and maintaining high fraction of Sn^0/Li_2O interfaces, is of great importance to achieve high reversibility of SnO_2 electrodes. By controlling the nanostructure of electrode and suppressing the Sn coarsening through the high density grain boundaries of SnO_2 nanocrystals, the conversion between Li_2O and SnO_2 can be highly reversible.

TOC:

Suppressing the Sn coarsening in Li_2O matrix enabled highly reversible conversion between Li_2O and SnO_2 and achieved an initial Coulombic efficiency of ~95.5%.

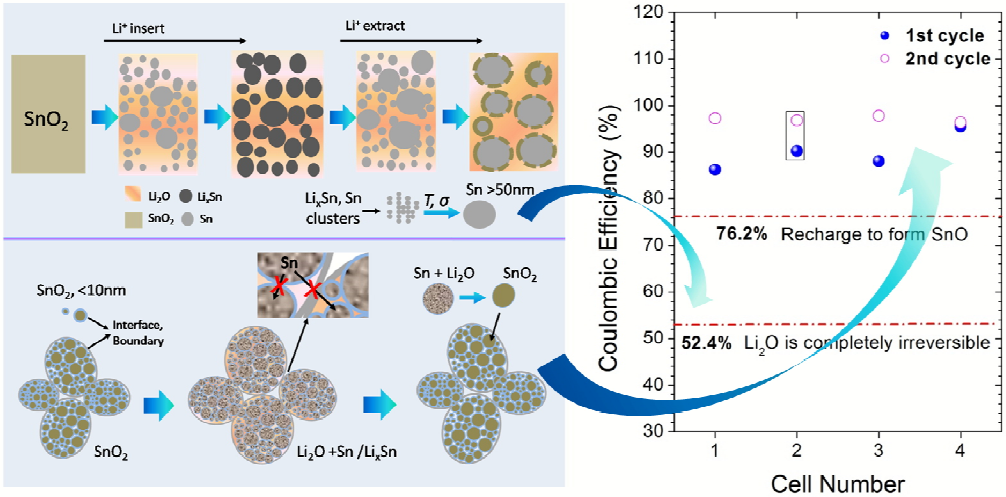

1. Introduction

The operation of intercalation based lithium-ion batteries involves Li^+ ion insertion into and extraction from the anode and cathode materials. Therefore, increasing the reversibility of Li^+ insertion and extraction is vital to achieving high energy density and long cycling life [1]. In particular, the reversibility of Li^+ extraction from lithium oxide (Li_2O), the formation of which contributes to the high capacity observed for oxide based anodes, has been a central issue in many lithium cells [2, 3]. Tin dioxide (SnO_2) has been considered one of the most promising anode materials [4-7]due to its high theoretical specific and volumetric capacity for Li storage in comparison with intercalated graphite and metal oxides (MO_x). Previous *exsitu* and *insitu* studies [8-11] suggested a two-step lithiation process for SnO_2 (Fig.1), a conversion reaction (Step I),

$$SnO_2 + 4Li^+ + 4e^- \rightarrow Sn + 2Li_2O,\ \sim 711 mAh/g,$$

followed by an alloying reaction (Step II),

$$Sn + 4.4Li^+ + 4.4e^- \leftrightarrow Li_{4.4}Sn,\ \sim 783 mAh/g.$$

Although there was little reported evidence of Li_2O formation due to its poor crystallinity, and thus difficulty in identification by X-ray diffraction (XRD) or electron diffraction under a transmission electron microscope (TEM), the conversion reaction that produces Li_2O has long been believed irreversible because of the following two observations. First, very large initial capacity losses (~50%, Fig.2) were universally observed for different types of SnO_2 electrodes[4, 6-8, 12]. Second, metallic Sn rather than an SnO_2 phase was detected when fully charged (as Li^+ was extracted)[7-9, 13].*Insitu* TEM observations of the lithiation process of a single SnO_2 nanowire (diameter>100nm) electrode further cemented the viewpoint that the reaction product, Li_2O, does not participate in reversible energy storage[14]. Accordingly, the irreversibility of Li_2O in SnO_2 and other oxide based anodes was identified as a critical challenge for achieving the limit of the

electrode capacity[15, 16]. In Li-O_2 batteries, similarly, the reversibility of Li_2O is very poor and the formation of Li_2O is believed detrimental to capacity retention and operational life. Thus, understanding how to make Li_2O fully reversible may also considerably enhance the capacity of Li-O_2 batteries.

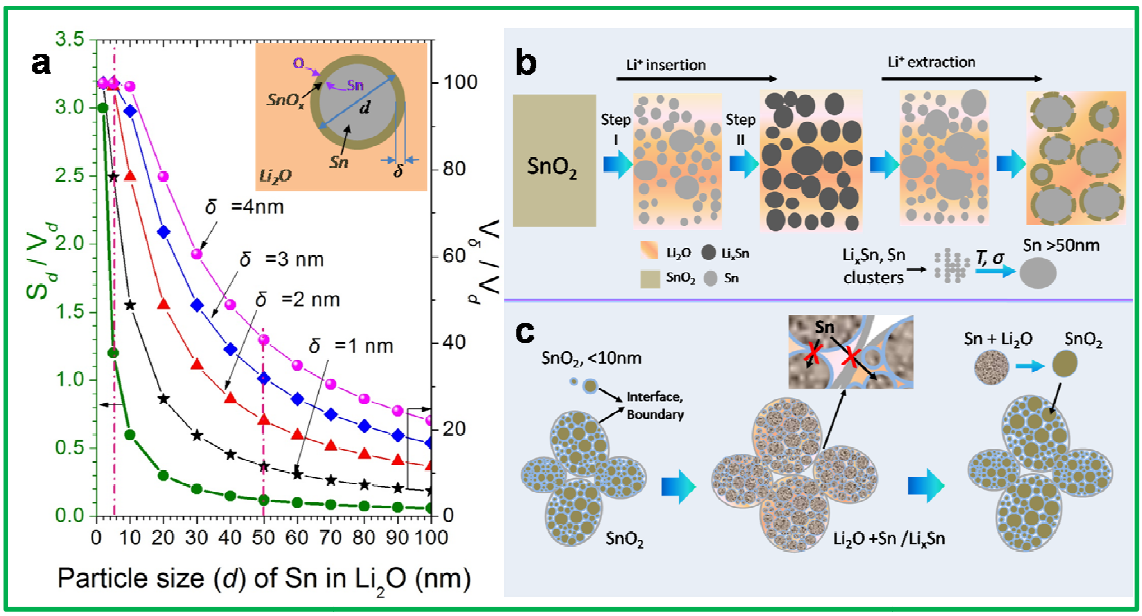

Fig. 1 Microstructure design for SnO_2 electrodes. **(a),**The relationship of S_d/V_d (left side) and V_δ/V_d (right side) with particle size (d) of Sn in a Sn/Li_2O mixture, where d, V_d and S_d represent the diameter, volume, and surface area of the spherical Sn particles, respectively, while δ and V_δ are the thickness and volume of the formed SnO_x layer, respectively. Right top inset illustrates the interaction of Sn and Li_2O during Li^+ ion extracting, where SnO_x formed at the interface of Li_2O and Sn by interdiffusion of O and Sn. **(b),** Schematic drawing shows the structure and phase evolution of a SnO_2 based electrode during initial discharge and charge, featuring the formation of Sn and Li_2O as well as subsequent Li-Sn alloying as Li^+ is inserted during discharge, and highlighting the processes as Li^+ is extracted during charge: dealloying of Li_xSn to form large Sn particles due to thermally-induced recrystallization and coarsening of Sn clusters[9, 17], leading to less Sn/Li_2O interdiffusion and smaller fraction of regenerated SnO_x.**(c),** Schematic diagram for structure evolution of hierarchical SnO_2.The large amount of interfaces and grain boundaries may prevent the Sn/Li_xSn coarsening, retaining the nanostructures important to complete conversion of Sn and Li_2O to SnO_2 after charging. (For conciseness, the Sn/Li_xSn networks and possible pathways for electrons transport were not shown. A schematic to show the proposed electron and Li^+ ion pathways in the nanostructured Sn/Li_2O is shown in the supplementary Fig.S5).

It is well known that MO_x electrodes such as CoO (with formation enthalpy ΔH of -238kJ/mol and Gibbs free energy ΔG of -214kJ/mol at 298K, ref.[18]) forms Co and Li_2O during lithiation. In the reverse direction, as Li^+ is extracted, the metal phases (M^0) and Li_2O can be

converted back to MO if the metallic grains are on the nanoscale (1-5nm), even though the bulk phase of Li_2O is more stable than MO_x thermodynamically (ΔH=-598kJ/mol, ΔG= -561kJ/mol)[19]. *Insitu* TEM observations revealed that the oxidation of M^0 to MO mainly involves interdiffusion near interfaces between M^0 and Li_2O[20-22]. However, in the M^0/Li_2O with larger transition metal M^0 particles, not only the kinetics of the conversion reaction were reduced but also a part of M within the large particles could not react with Li_2O and remained in the elemental state[22], indicating the importance of maintain nanosized metal particles for high reversibility of the conversion reaction in metal oxide anodes[23]. If this logic also prevails in a SnO_2 based electrode, Li_2O could also react reversibly with Sn to form SnO_2 (ΔH=-581kJ/mol, ΔG=-520kJ/mol), provided that the Sn^0/Li_2O mixture in the lithiation products has proper nano-sized interfacial structure. The Gibbs free energy change ($\Delta_r G_m^{(\theta)}$, at 298K) for the conversion reaction of SnO_2 anode during lithiation (Step I) is calculated to be about -602kJ/mol, while that for the CoO anode is about -347kJ/mol. These indicate that, the Sn/Li_2O mixture needs to overcome a large energy barrier of ~602kJ/mol when Sn and Li_2O react to form SnO_2 again during de-lithiation, which is much higher than that of ~347kJ/mol for the conversion of Co/Li_2O to CoO. This should be one of the reasons why the conversion of transition metal oxide (e.g., CoO) anodes is generally easier than that of the SnO_2-based anodes. Nevertheless, compared with the transition metals, Sn has larger atomic volume ,much lower melting point (T_M of ~506K) and extremely low temperature for recrystallization (T_R, ~224K, simply estimated from equation of T_R=0.4T_M). Accordingly, unlike the stable transition metals (with high T_R, *~707K*for Co), nano-sized Sn phases tend to coarsen to larger particles even at room temperature. Furthermore, the Sn and Li_2O are immiscible, and thus the Sn phase also tends to coarsen and migrate to the surface of Sn^0/Li_2O mixtures to minimize the surface/interface energy[24, 25].These lead to reduced Sn/Li_2O

interfaces and an accordingly shorter length interdiffusion layer (*i.e.* restored SnO_x). In addition, the solid-electrolyte interphase (SEI) film formed on the expanding and contracting surfaces of Sn particles during Li-Sn alloying and de-alloying could also isolate the Sn and Li_2O, resulting in low reversibility for conversion reaction[26].

2. Results and Discussion

2.1 Design and fabrication of nanostructured SnO_2

Large Sn particles have poor reversibility (Fig.1, a and b).The rapid coarsening of Sn and Li_xSn to form large particles (d>50nm) has been observed under *exsitu* /*insitu* conditions in nanocrystalline SnO_2 thin films and single SnO_2 nanowire electrode[7-9]. Although no obvious aggregation and larger Sn clusters was found in a ~3nm SnO_2 nanoparticle electrode after 30 cycles, the low cut-off potential (1.2V) applied during charge prevented the conversion reaction of Li_2O and Sn to SnO_2 [27]. Simple calculation suggests that, for an electrode consisting of spherical Sn particles with d=50nm and δ=3nm (Fig.1a), the volume fraction of the interdiffusion layer is only 31.8% of the large Sn particles (i.e., $V_\delta / V_d = 31.8\%$), implying that no more than ~31.8% of the SnO_x phase may be reversible. As schematically illustrated in Fig. 1a and c, however, if the Sn particle size is controlled at d=5nm and the interdiffusion layer thickness at δ =2nm, the volume fraction of the interdiffusion layer would be increased to 99.2% of the Sn particles (i.e., $V_\delta / V_d = 99.2\%$), implying that almost all the SnO_x phase may become reversible. Clearly, it is critical to create nanostructured electrodes that have a large volume fraction of interfaces between Li_2O and nanosized M^0 to enhance the reversibility of Li_2O in an oxide-based electrode.

To demonstrate that the reversibility of Li_2O in a SnO_2 based electrode depends on the nanostructure of the electrode (especially that of the Sn^0/Li_2O mixture in the lithiation products), we constructed a thin-film SnO_2 electrode (Fig.1 c) with a large amount of interfaces and grain boundaries by magnetron sputtering. This model electrode has a clean vacuum-sputtered surface with very low specific surface area ($0.98 m^2/g$ from BET, Supplementary Fig.S1) which reduces other irreversible lithium-consuming complications which were very common in the SnO_2 nanocomposite with high surface area[27]. The high initial Coulombic efficiency (ICE, up to 95.5%) and large capacities of the SnO_2 film electrode are attributed to the excellent reversibility of Li_2O formation/decomposition during cycling.

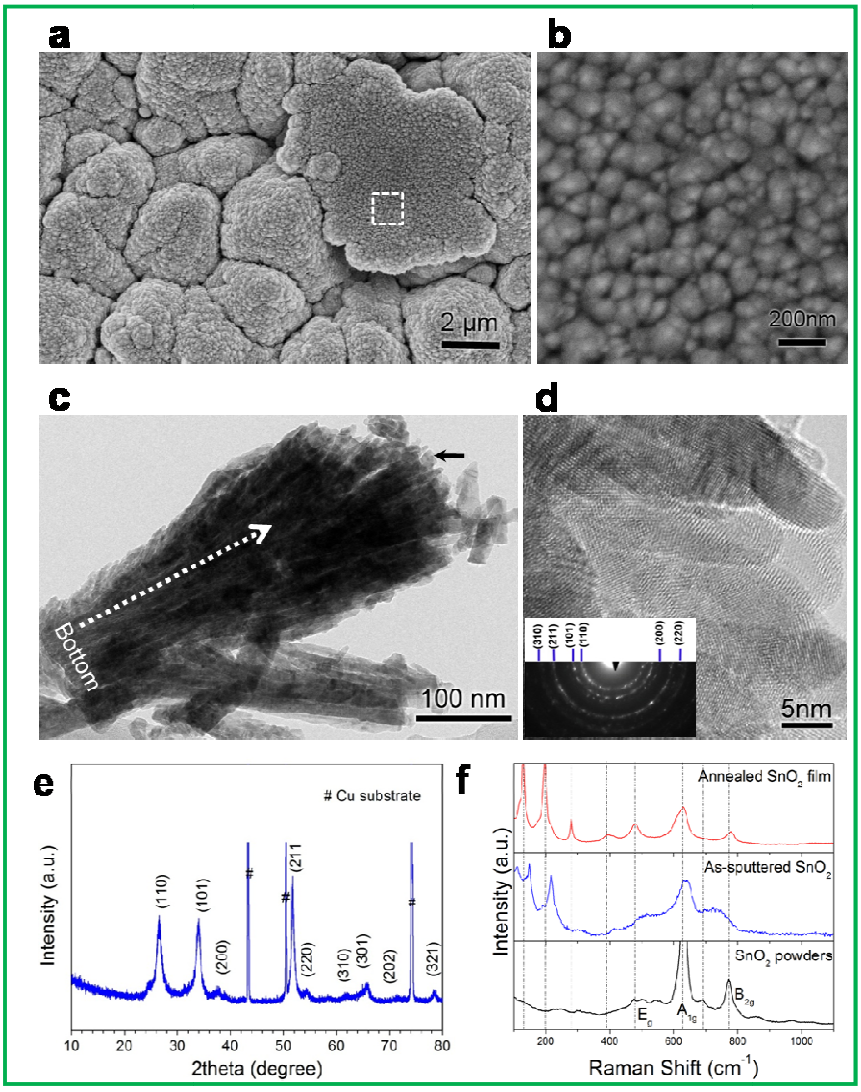

Fig. 2 Microstructure and phase characterization of the nanostructured SnO_2 thin film prepared by magnetron sputtering.(**a),** Top-view morphology (SEM images) of as-sputtered film on Cu foil sustrate; the SnO_2 layer is transparent (see Supplementary Fig.S2).(**b),** Enlarged image for zone outlined in (a). **c,**Low magnification TEM image of a part of the SnO_2 bundles scraped from the film. (**d),** A HRTEM image from the zone arrowed in (c) showing obvious boundaries of the rod-like nanocrystals,all the diffraction rings of inset electron-diffraction partten can be indexed as the tetragonal SnO_2. (**e),** XRD pattern of the SnO_2 film, a small amount of preferred orientation along the *c*-axis to form plates was observed by Rietveld refinement (see Supplementary Fig.S1). (**f),** Raman spectrum of the SnO_2 film in comparison with that of a commercial SnO_2 powder (with particle size less than 10μm) (see Supplementary Fig.S2).

Fig.2a and 2b show some typical scanning electron microscope (SEM) images of an as-sputtered SnO_2 film, where the spherical SnO_2 particles of ~2 to 5μm in diameter are actually aggregations of small nano-sized grains (about 100 nm) with a large amount of interfaces among the small

SnO_2 crystallites. A cross-sectional view of the deposited transparent SnO_2 layer(~900nm thick, Supplementary Fig.S2) reveals that each nano-sized grain (Fig.2b) is actually composed of many ultrafine nano-columnar SnO_2 crystallites, as more clearly seen in the TEM and STEM images (Fig.2c, Supplementary Fig.S2). Most of the boundaries among the columns cross throughout the SnO_2 layer. The obvious nano-, micro-, and macro-columns, together with a large amount of associated nano-, micro, and macro-voids of this SnO_2 film is drastically different from those of the previously reported SnO_2 film electrodes[7, 8, 28, 29], which generally had a compact structure of disordered grains of 50 to 200 nm in diameter. The electron diffraction pattern and lattice image (Fig.2d), together with the XRD pattern (Fig.2e) and its Retieveld refinement (Supplementary Fig.S1), confirm that the ultrafine nano-crystallites are tetragonal SnO_2.The average crystallite size of SnO_2 is estimated to be ~9.5nm with a small amount of preferred orientation along *c*-axis to form plates. Raman spectroscopic analysis indicates (Fig.2f) that, although the A_{1g} mode for SnO_2 phase remained similar, many spectral features (e.g., the E_g and B_{2g} modes) of this SnO_2 film are different from those of a SnO_2 powder sample. The SnO_2 powders have an E_g peak at 479cm^{-1} and B_{2g} at 774 cm^{-1}, however, for the as-sputtered SnO_2 film, the E_g shifted to about 540cm^{-1} while the B_{2g} shifted to about 750cm^{-1}. This is likely due to the unique nanostructure of the SnO_2 film, including the strains and stresses induced during film growth and /or the preferred orientation of the SnO_2 nanocrystals[30, 31].This is corroborated by the fact that the spectral features (both E_g and B_{2g} modes) of an annealed SnO_2 film became similar to those of the SnO_2 powder sample (Fig.2f, Supplementary Fig.S2).It has been found that, annealing of the sputtered SnO_2 leads to grain boundary fusing and the SnO_2 layer densifying with less boundaries among the nano-columns. The voids among the macro/micro-columns found in the as-prepared sample have collapsed as the nanosized SnO_2 grains fused to form a dense film. These resulted in much lower

ICE (70.9%) in the annealed film (Supplementary Fig. S3). Furthermore, a much thinner SnO_2 layer (~9nm thick), which is dense and lacks the columnar structure, also had a bit lower ICE of about 82% (Supplementary Fig. S4). These suggest that the unique multiscale columns and the void distributions, together with the ultrafine SnO_2 nanocrystals, are of importance to the high reversibility of the SnO_2 film. Specifically, the gaps between grains, interfaces, and grain boundaries may significantly influence the transport of Sn, impeding the diffusion (in the direction perpendicular to the interfaces and grain boundaries, ref. [32]) from one grain into another during lithiation /delithiation (Fig.1c). As a result, a film composed of SnO_2 nanocrystals of ~9.5nm maintained ultrafine Sn particles (revealed by XRD, Fig.4b) in the Sn/Li_2O mixture, leading to almost completely reversible conversion between Li_2O/Sn and SnO_x/Li (Step I) during cycling.

2.2 Dramatically enhanced initial Coulombic efficiency

The electrochemical performance of this nanostructured SnO_2 film was evaluated (Fig.3, a to f) in Li-SnO_2 half cells. Shown in Fig.3a and Supplementary Fig.S5 are some initial discharge/charge cycling curves of four cells discharged from open cell potential (OCP) to 0.01 V(vs. Li/Li^+) and then recharged to 3V, indicating that about 86.2% to 95.5% of the initial capacities were retained in the second cycle. The ICE for the four cells tested ranged from 86.2 to 95.5%, much higher than the theoretical value of 52.4% when Li_2O is completely irreversible (Fig.3d), and among the highest value reported so far for pure SnO_2 and SnO_2-based hybrid electrodes [4, 6-8, 33]. Presented in Fig.3c are the capacities of the first and the second discharges of these four cells, showing that they are much higher than the capacity corresponding exclusively to the conversion reaction (711mAh/g) or that the alloying reaction (783mAh/g) shown in Fig.1 and Fig.3. It should be emphasized that the differences in capacity and ICE among these four

cells (Fig.3, c and d, Supplementary Fig.S5) are attributed to the differences in the nanostructures of the sputtered SnO_2 films. These differences mainly existed among the very initial potential range from OCP to 1.2V, which is usually attributed to the SEI formation on the electrode surface and the initial lithiation of SnO_2. The amount of the SEI formed on the nanostructures and the lithiation extent of the SnO_2 would affect the initial discharge/charge capacities and the ICEs. As shown in Fig.2, the surface morphology and the SnO_2 columns could not be completely uniform in the four different electrodes. And thus, the electrode with a bit higher surface area and slightly larger SnO_2 grains would result in a lower initial Coulumbic efficiency, just as shown in the annealed film and other thin films (Supplementary Fig.S3, Fig.S4). Nevertheless, the additional reversible capacities and the high ICE must include significant contribution from the reversible conversion between Li_2O/Sn and SnO_x/Li (Step I) during cycling.

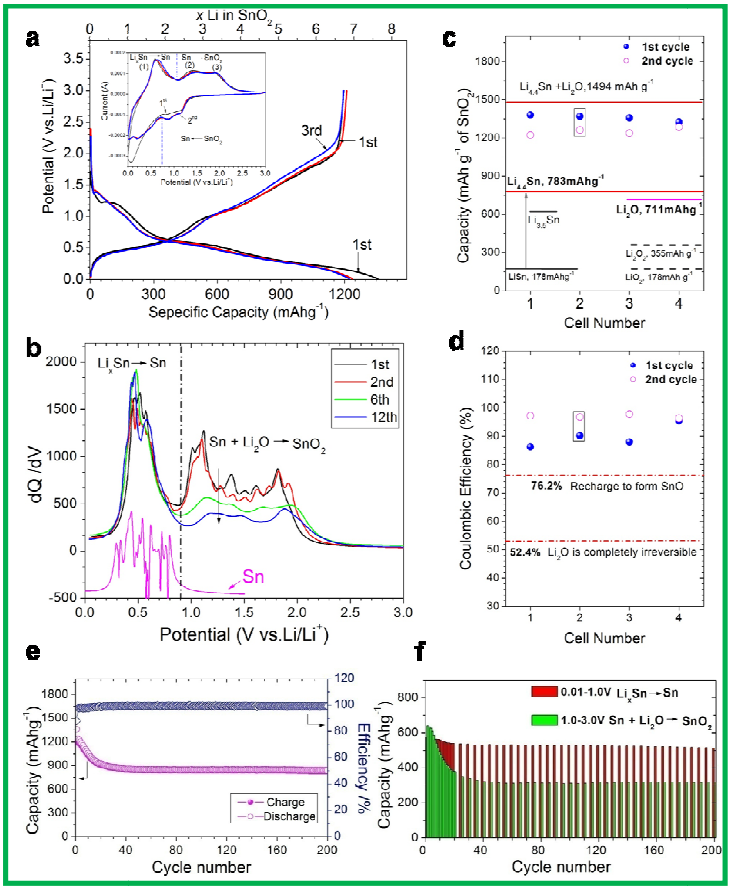

Fig. 3 Electrochemical properties of four SnO_2 film electrodes in Li/SnO_2 half cells tested between 0.01 and 3V. The electrolyte was 1M lithium hexafluorophosphate ($LiPF_6$) in mixtures of ethylene carbonate: dimethyl carbonate (EC: DEC) =1:2 in weight with 10wt% of FEC (Fluoroethylene carbonate).Acitve SnO_2 loading on Cu foils was around 0.40mg/$cm^2$with a 0.9 μm thickness and relative density of 70% in comparision with the theoretical density of SnO_2 (6.4 g/cm^3).**(a),**Discharge-charge curves for the first three cycles of cell #2 at current rate of 1/5C where 1C=1494mA/g. Inset shows the first twoCV curvesobtained from another cell. (**b),** Differential charge capacity curves *vs.* voltage of SnO_2 electrode at the 1st, 2nd, 6th and 12th cycle. Left bottom inset is that of pure Sn film. (**c, d),**Summary of the 1st and 2nd discharge capacties and Coulombic efficiencies (CE) for the fourcells. Theoretical specific capacities (based on mass of SnO_2) and CE for different phases were presented as a reference. **e,** Cycleability of cell #2 at 1/5C rate, with 70% of the initial reversible capacity retained after 200 cycles. (**f),**Reversible (charge) capacities *vs.* cycle number seperated from potential range of 0.01-1.0V and 1.0-3.0V.

This can be confirmed by the initial discharge-charge curves (cell #2, ICE = 88.1%) and cyclic voltammograms (CV) of the SnO_2 electrodes in comparison with those of a pure metallic Sn electrode (Supplementary Fig.S5). The conclusions drawn from electrochemical testing are corroborated by XRD, TEM, and *insitu* surface-enhanced Raman spectroscopy (SERS, Fig.4,

Supplementary Fig.S6, Fig.S7). From Fig.3a and Supplementary Fig.S5, we can see that the SnO_2 electrode had a long-sloping plateau during delithiation and the reduction peaks in the CV were broadened (inset) at potentials greater than 1.0V (vs. Li/Li^+), which is attributed to the reversion of Li_2O to SnO_2. These features are absent from similar plots for the SnO_2 anodes with poor reversibility. Specifically, the current in CV curves of the 1st cycle at potential of 1.3-0.7V is a bit lower than that of the 2nd cycle. However, the current of the 1st cycle at potential of 0.4-0.01V is much higher than that of the 2nd cycle. As a result the peak current (also capacity in mAh) in the 1st cycle is higher than that at the 2nd cycle, which is consistent with the capacity-potential curves showing a small amount of irreversible capacity loss in the 1st cycle. The Li^+ diffusivity (D_{Li+}) in the SnO_2 film electrode during the conversion of Li_2O to $SnO_2$was estimated (from the corresponding CV curves shown in Supplementary Fig.S5) to be ~$10^{-13}cm^2/s$, which is about two orders of magnitude smaller than that during the Li_xSn de-alloying process ($10^{-11}cm^2/s$). However, it is much greater (Supplementary Table S1) than those reported for an amorphous lithitated SnO_2 nanowire (10^{-16}-$10^{-14}m^2/s$)[14] and an amorphous lithiated SnO_2 film (10^{-15}-$10^{-13}m^2/s$)[29]. This should be attributed to the high fraction of Sn/Li_2O interfaces in the ultrafine grains, which enhanced the kinetics of Li^+ migration in the Li_2O matrix (Supplementary Fig.S5). Similarly, inside the Li_2O matrix the ultrafine Sn and Li_xSn would form connected networks and serve as the conduction pathways for electrons[22]. The estimated diffusion distance for the conversion of Li_2O to SnO_2 (from 1.0 to 3.0V) under the applied current was >70μm, much larger than the thickness of the SnO_2 layer (Supplementary Table S1).This explains why the conversion between Li_2O and SnO_2 was largely reversible in the first several discharge/charge cycles. However, the reversibility of the conversion reaction degraded during cycling, as reflected by the differential capacity curves (Fig.3b) in which the height of the peaks

for conversion of Li_2O to SnO_2 diminished gradually with the number of cycles, indicating capacity fading in the potential range of 1.0-3.0V over time. As shown in Fig. 3f, the reversible capacities between 0.01-1.0V remain stable among 200 cycles, while the capacity in the 1.0-3.0V range declined most rapidly during the initial 20 cycles and the variation of capacity in this region during cycling is quite similar to the total capacity of SnO_2. These indicated that the capacity fading of the SnO_2 electrode occurred mainly in the potential range of 1.0-3.0V, due to the reversible fading for conversion of Sn/Li_2O to SnO_2. The fading of reversibility for conversion reaction should be due to the unavoidable grain boundary damage and thus gradual Sn coarsening in the Sn/Li_2O mixture during the first several cycles (Supplementary Fig.S8). Still, this SnO_2 film electrode retained a stable capacity of ~800 mAh/g over 200cycles (Fig.3e), which is comparable to those of the most complex design of nanostructured SnO_2 and hybrid electrodes[6, 25, 33-35].These high reversible capacities indicated that not only the SnO_2 nanocrystals near the surface but also those inner of the film could fast react with Li^+. The obvious nano-, micro-, and macro-columns, together with the associated nano-, micro, and macro-voids, were helpful for the fast transport of electrolyte and Li^+ among the SnO_2 nanocrystals. The voids among the micro/nano-columns acted as the free-spaces to effectively accommodate the volume change of SnO_2 during Li insertion and extraction and thus remained the good structure integrity and high capacity retention in SnO_2 layer. This demonstrates the significant effect of nanostructure on the reversibility of battery chemistry and the structural stability of conversion-type electrodes.

2.3 Confirmation of Li_2O reversiblilty

In order to confirm that the highly reversible formation and decomposition of Li_2O in the SnO_2 electrode, we first colleted *exsitu* XRD data at five different discharge/charge states during the

first cycle (Fig.4, a and b). During discharge, the initial SnO_2 phase was slowly transformed to metallic Sn and the transformation was complete at a discharge potential of~0.56V (vs. Li/Li^+). The formation of Li_xSn phase was then observed at the end of discharge (~0.01V), consistent with the previvous studies[3, 9, 14].In stark contrast, not all the diffraction peaks corresponding to the Li_xSn and the Sn phases were observed during the re-charge processuntil the cutoff potential (~3.0V), even after the first 5 cycles (Fig.4, b and f). Instead, we observed a broad hump in the diffraction pattern (in a 2θ range of 15~25^o) and a diffuse ring electron diffraction pattern (Fig. 4c), suggesting that the fully-charged electrode is amorphous. Since a metallic Sn phase generally can not be amorphous at room temperature, it must be composed of amorphous Sn-based oxides, which still retained similar initial nanostructure as revealed by the STEM image (Fig.4d). Furthermore, the observed morphology after cycling is quite different from those of the previously reported SnO_2 electrodes. There were no obviously larger Li_xSn or Sn particles /aggregations in this fully lithiated SnO_2 film electrode (first discharge to 0.01V). As shown in Supplementary Fig.S9, the electron diffraction pattern confirmed the existence of the Li_xSn nanocrystals, which were ultrafine in size and homogenously dispersed inside the Li_2O matrix. However, the fully lithiated SnO_2 were unstable even at short exposure of electron beam due to the presence of ultrafine Sn and Li_xSn phase (Supplementary Fig.S8). Although the electron energy loss spectroscopy (EELS) signals from O K-edge and Sn M-edge are partly overlapped, as shown in Fig. 4e**,** both of the Sn M-edge and O K-edge in the electrode after charge to 3.0V are similar to those of pristine SnO_2 film, suggesting that the Sn would have similar oxidation state in the two samples. The existence of dominant SnO_2 in the charged electrode was also confirmed by X-ray photoelectron spectroscopy (XPS) (Supplementary Fig.S8),with the same binding energies for Sn $3d_{5/2}$ and $3d_{3/2}$ as in the as-sputtered SnO_2 film (Supplementary

Fig.S10).These results suggest that all the metallic Sn in the lithiated film electrode was completely re-oxidized to amorphous SnO_2 as Li^+ was extracted; this reversible conversion between Li_2O and SnO_2 is responsible for the demonstrated higher capacity, which has not yet been observed or reported in previous studies of other SnO_2 based electrodes[8-10, 13, 14].

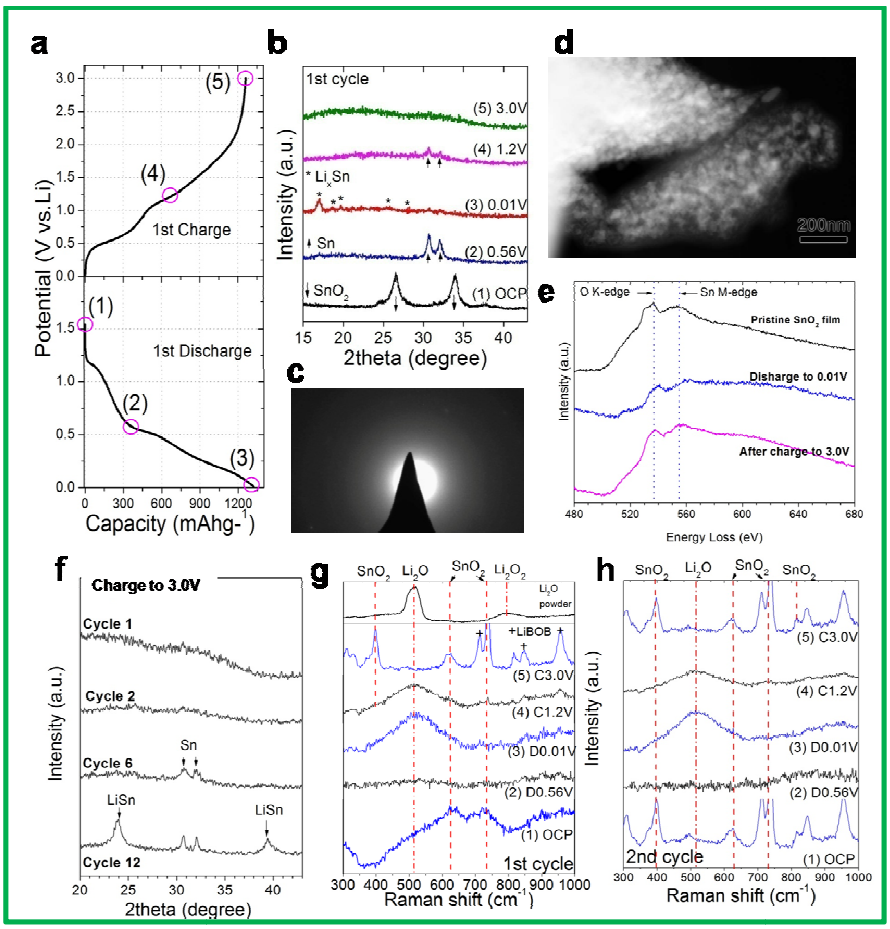

Fig. 4 Characterization for microstructure and phase evaluationof the SnO_2 film electrode during discharge and charge by *exsitu* and *insitu* methods. (**a),**Initial potential *vs.* capacity curve of the Li/SnO_2 half cell marked with five lithiated states for microstructure examinations, namely OCP, discharged to 0.56 and 0.01V, recharged to 1.2 and 3.0V. (**b),***Exsitu* XRD patterns for the SnO_2film electrode at fivedifferent states for the first cycle. (**c,d),** EDP and STEM image of the SnO_2 recharged to 3.0V at the first cycle, respectively. **e,**Core-loss EELS from a large area of the the SnO_2 sample after the 1stdischargeing to 0.01V, recharging to 3.0V and the pristine film, in which both of the Sn M-edge and O K-edge in the electrode after charge to 3.0V are similar to those of pristine SnO_2 film, suggesting that the Sn would have similar oxidation state in the two samples. (**f),**Comparison *ex-situ* XRD partterns for the SnO_2 electrode at the state of recharging to 3.0V after different cycle (1st, 2nd, 6th, 12th). (**g, h),** *Insitu* SERS spectra of the SnO_2 film electrode recorded at different states. (g) and (h) is for the first and the second cycle, respectively.1M Lithium bis(oxalato)borate (LiBOB) in propylene carbonate (PC)electrolyte was used in Raman testing cells.

To further corroborate the reversible conversion between Li_2O and SnO_2, we performed *insitu* SERS of the electrode (Fig.4g and 4h) in a specially-designed cell with a quartz window (Supplementary Fig. S11).The Raman spectrum at 1st OCP showing lower peak intensity for SnO_2 was due to the covering of electrolyte on the film surface. A series of *insitu* SERS spectra collected at different cycling states (Supplementary Fig. S6, Fig.S7) clearly demonstrate the disappearance and regeneration of the SnO_2 and the Li_2O phase during cycling, providing the strongest evidence to support the conclusion that the conversion between Li_2O and SnO_2 is reversible during the discharge/charge cycle. Fig.4g and 4h show the SERS data recorded at the desired potential points (Fig.4a) for the first and the second cycle, respectively. The characteristic peak for Li_2O at ~520 cm^{-1} was observed at the end of each discharge, but was absent from the spectrum at the end of each charge. In contrast, the peaks for SnO_2, in addition to the peaks arising from the LiBOB salt (Supplementary Fig.S12), were apparent in the end of charging to 3.0V. It had been found that at the end of charge, the regenerated SnO_2 presented narrower band widths in the Raman spectrum. This could be due to that, in some zones, the regenerated nanosize SnO_2 had a good crystalline and was free of stress and orientation structure. Furthermore the broad Raman peak of Li_2O is found to be more similar to that of the Li_2O formed on the surface of a lithium foil (Supplementary Fig.S12), rather than that of a micro-sized Li_2O powder, due most likely to its fine nano-structure or amorphous nature of the lithiated SnO_2 electrode [14, 20, 22]. The variation in intensity of the peaks for LiBOB may be attributed to the morphology change of the film due to the volume expansion and contraction of the SnO_2 layer (Supplementary Fig.S13).

Clearly, the reversibility of Li_2O in the Sn/Li_2O mixture is closely related to the nanostructure of the electrode. In this unique SnO_2 film, the interfaces and grain boundaries may

effectively suppress the coarsening of the Sn phase in Li_2O, thus maintaining the high activity for inter-diffusion between Li_2O and Sn required for reversible inter-conversion. The obvious nano-, micro-, and macro-columns, together with the associated nano-, micro, and macrovoid distributions, were helpful for enhancing the reaction kinetics and structure intensity in the SnO_2 layer. As expected, another as-sputtered SnO_2 film electrode (Supplementary fig.S14) with larger grains and less grain boundaries showed inferior reversibility (ICE=69.1%). Although the capacity deterioration of the pure SnO_2 electrode is still a challenge due to gradual Sn coarsening during the first several cycles (Fig.4f, Supplementary Fig.S8), it must be noted that highly reversible Li_2O was realized by carefully tuning the nanostructure to maintain high fraction and well connected interfaces of Sn/Li_2O in the electrodes. Our recent efforts have produced nanostructured electrodes with highly reversible conversion between Li_2O/Sn and SnO_x/Li for up to 200 cycles.

Considering the similar situation in a Li-O_2 battery[3], the highly reversible Li_2O in Li–SnO_2 cells imply that a well-designed O_2 electrode for a Li-O_2 battery may effectively utilize the high capacity Li_2O, which has far greater capacity than that of Li_2O_2. For example, a hierarchical porous carbon electrode loaded with metal and/or oxide catalysts (Supplementary Fig.S15), with high activity/mass ratio and high activity/cost ratio, may facilitate selective formation of Li_2O on the surface of the catalysts during discharge and reversible decomposition of Li_2O upon charge at modest potential, thus providing higher energy density and greater roundtrip efficiency in Li-O_2 batteries.

3. Conclusion

Our results demonstrate that the conversion between Li_2O and SnO_2 can be highly reversible if a proper nanostructure is maintained, providing new insight into the rational design of highly

reversible Li_2O-containing electrodes in Li-SnO_2 cells. We have directly observed repeatable formation and decomposition of nanostructured Li_2O under *insitu* conditions, demonstrating high reversible capacities of electrode over 200 cycles. Although this work was carried out for a SnO_2 film electrode, the material tuning strategies and experiments are applicable to other metal oxide electrodes, especially Li-O_2 batteries, where the reversible capacity and energy density are limited by the irreversibility of Li_2O. We believe the results presented here provide a new understanding of metal-oxide anodes and encourage us to fully exploit other potential ultrahigh-capacity storage materials for Li-ion and Li-O_2 batteries.

4. Experimental

4.1 Preparation of SnO_2 thin film electrodes:

The SnO_2 thin film were deposited on battery grade Cu foil (thickness: 12μm, area: 6×6cm^2) using a KYKY (China) JGB-560 high vacuum magnetron sputtering system. The SnO_2 target (diameter 60mm, purity of 99.9%) was sputtered using a radio frequency (RF) magnetron under optimized parameters (150W, 30minutes). SnO_2 thin film with shorter sputtering time (18 seconds) was also prepared (Supplementary Fig.S4). The distance of target surface to Cu substrate was 10cm. There was not heating or rotating for the substrate holder during sputtering. After 2.0×10^{-4} Pa base pressure was achieved, 2.0Pa Ar (purity of 99.99%), with a constant flow of 20sccm, was used as the working gas during deposition. The sputtered SnO_2 layer looks like colorless transparent glass.

The mass of deposited SnO_2 was determined by weighing the substrate before and after sputtering deposition of SnO_2 using an FA1104N balance. Accordingly, the weight of the active SnO_2 in the film electrode was calculated to be around 0.4 mg/cm^2.It is found that the thickness of the SnO_2 layer is not completely homogenous due to the absence of rotation for the sample

holder. This SnO_2 film was annealed in Ar at 500^oC for 4 hours and also investigated as electrode for comparison. We need to point out that the sample with rotation during sputtering presented quite different morphology and inferior reversibility (Supplementary Fig.S14), which would not be discussed in detail in this work.

In order to prepare the sample for *insitu* surface enhanced Raman spectroscopy (SERS) measurement, ultrafine Ag nanoparticles were deposited on the surface of the as-prepared SnO_2 film by direct current magnetron sputtering (8W, 2min, Ar 2Pa).

4.2 Structural Characterization:

X-Ray Diffraction (XRD) was performed on a PANalytical X'Pert PRO Alpha-1 diffractometer equipped with monochromatic Cu-K$\alpha 1$ radiation operating at 45kV and 40mA. The surface and cross-section morphologies of the as-prepared thin film were examined using LEO 1530 scanning electron microscopy (SEM). Transmission electron microscope (TEM) observations were conducted in a FEI Tecnai F30 microscope operating at 300kV, fitted with STEM and EELS units. For TEM analysis, the SnO_2 fragments were scraped from the substrate and directly dispersed on carbon-coated Cu grids. Raman spectra were obtained using a Renishaw RM 1000 spectromicroscopy system (~2μm spot size) equipped with a 20 X objective optical micrscope. An air-cooled Ar laser with a 488nm wave length was used for excitation of the Raman signal in this study with a total power of 10mW. Raman analysis of Li_2O powder, Li foil, and Lithium bis(oxalato)borate (LiBOB)-PC electrolyte was undertaken by placing the samples in the sealed chamber with a quartz window prepared within the Ar-filled glovebox.

For the *ex situ* XRD /TEM /XPS studies, the SnO_2 electrodes after cycling were carefully stored and transferred to minimize air exposure. SnO_2 film electrode at different lithiatied states were

prepared by controlling the discharge/charge cutoff voltage during the electrochemical reaction. The "Swagelok" cells were disassembled inside of an Ar filled glovebox after cycling to take out the electrodes, which were rinsed with DMC and absolute ethanol and then dried under vacuum in the chamber of glove box. For XRD measurement, the reacted SnO_2 film electrodes were sealed inside Kapton tape to minimize air exposure during the measurement. For TEM observation, the reacted SnO_2 layer was scraped off the Cu substrate and directly dispersed on carbon-coated Cu grids inside the glove box. The samples transferred to TEM and XPS were stored in a small box filled with Ar to minimize air exposure. Before XPS survey, the surface of the samples were etched by Ar ion beam for 30s.The binding energy scale of XPS was calibrated from the carbon contamination using the C 1s peak at 285.0 eV.

The Rietveld refinement of XRD parttern was carried out to evaluate the crystallite size and oriatetion for the SnO_2, by using a pseudo-Voigt profile function with a profile base with the value of 8. The background was first deternined with an automatic Sonneveld-Visser algorithm and then fixed during the refinement.

4.3 Electrochemical measurements:

The electrochemical performance of the obtained thin film electrodes was investigated with half-cells assembled in argon-filled glove boxes (O_2, H_2O levels maintained at <1ppm). The as-sputtered thin films were directly used as working electrodes. Lithium ribbon and polyethylene membrane (Celgard 2325) were used as the counter electrode and separator, respectively. The electrolyte (Tinci Corporation) was 1M $LiPF_6$ in mixture of 1:2 by weight ethylene carbonate: dimethyl carbonate (EC: DEC) =1:2 with an additional 10wt% of Fluoroethylene carbonate (FEC). Most testing cells were CR2016 coin-type cell configuration, but for the electrodes characterized *ex*-situ using XRD and TEM, "Swagelok" cells were used due to the ease of

disassembly. After cells were assembled they were aged overnight before electrochemical testing. The galvanostatic charge–discharge cycling tests were conducted on a CT2001A (LAND, China) and BT2000 (Arbin Instruments, USA) battery test systems at current density of C/5 rate (equal to around 100μA/cm^2) over a voltage range of 0.01–3V vs. Li/Li$^+$ at room temperature. The specific charge/discharge capacities of the film electrodes were calculated by using the overall capacity of electrodes divided by the weight of the active SnO_2 layer. Cyclic voltammetry (CV) was performed at different scanning rate (0.2, 0.3, 0.4, 0.6mV/s) from 0 to 3V.

4.4 *In Situ* SERS:

For *in situ* SERS observation, the Ag nanoparticles coated SnO_2film were acted as the working electrode in a spectroelectrochemical cell (MTI Cooperation). The picture for the cell and schematic for the inside configuration were shown in Supplementary Fig.S11. A small hole was made in the lithium foil and separator in order to observe the SnO_2 film surface.

Hwang et al. have reported their study about *insitu* SERS observation of Li_2O evolution on Li-rich $Li[Ni_xLi_{(1-2x)/3}Mn_{(2-x)/3}]O_2$ cathode materials[36], which was working with electrolyte of 1M $LiPF_6$ in mixtures of EC/DEC (1:1). However, we found there was serious fluorescence effect in case of $LiPF_6$ based electrolyte using for SnO_2 film electrode (Supplementary Fig.S12), which covered all the signals of SnO_2 and the discharge and charge products. Thus, we constructed Raman cells with electrolyte of 1M LiBOB in PC (propylene carbonate). In the latter case, the CV curves indicate that the lithiation/delithiation behaviors of SnO_2 in LiBOB are similar to those in $LiPF_6$ (Supplementary Fig.S5).

The *insitu* Raman cell were tested galvanostatically tested using a Solatron Analytical 1470E potentiostat. At the same time, an *insitu* time-resolved study was conducted by placing the laser

spot on the same location, with the laser slightly out of focus to cover a larger area of about 5μm in diameter.

Electronic supplementary information (ESI) available:

Supplementary figures (Fig.S1-15) and **Table** (Table S1).

Acknowledgments:

This material is based upon work supported as part of the Heterogeneous Functional Materials (HetroFoaM) Center, an Energy Frontier Research Center funded by the U.S. Department of Energy, Office of Science, Office of Basic Energy Sciences (DE-SC0001061), the US National Science Foundation (DMR-1410320), the National Science Foundation of China (No.51201065 and 51231003), the Doctorate Foundation of Ministry of Education (20120172120007), the Foundation for the Author of Excellent Doctoral Dissertation of Guangdong Province (SYBZZXM201309). Dr. Yong Ding'sTEM analysis is very much appreciated. RZ Hu was supported by a fellowship from China Scholarship Council (201406155009).

References

1. J. B. Goodenough and K.-S. Park, *Journal of the American Chemical Society*, 2013, **135**, 1167-1176.
2. H. B. Wu, J. S. Chen, H. H. Hng and X. Wen Lou, *Nanoscale*, 2012, **4**, 2526-2542.
3. A. Kraytsberg and Y. Ein-Eli, *Journal of Power Sources*, 2011, **196**, 886-893.
4. Y. Idota, T. Kubota, A. Matsufuji, Y. Maekawa and T. Miyasaka, *Science*, 1997, **276**, 1395-1397.
5. J. S. Chen and X. W. Lou, *Small*, 2013, **9**, 1877-1893.
6. R. Hu, W. Sun, H. Liu, M. Zeng and M. Zhu, *Nanoscale*, 2013, **5**, 11971-11979.
7. T. Brousse, R. Retoux, U. Herterich and D. M. Schleich, *Journal of The Electrochemical Society*, 1998, **145**, 1-4.
8. R. Retoux, T. Brousse and D. M. Schleich, *Journal of The Electrochemical Society*, 1999, **146**, 2472-2476.
9. C.-M. Wang, W. Xu, J. Liu, J.-G. Zhang, L. V. Saraf, B. W. Arey, D. Choi, Z.-G. Yang, J. Xiao, S. Thevuthasan and D. R. Baer, *Nano Letters*, 2011, **11**, 1874-1880.
10. H. Kim, G. O. Park, Y. Kim, S. Muhammad, J. Yoo, M. Balasubramanian, Y.-H. Cho, M.-G. Kim, B. Lee, K. Kang, H. Kim, J. M. Kim and W.-S. Yoon, *Chemistry of Materials*, 2014, **26**, 6361-6370.
11. I. A. Courtney and J. R. Dahn, *Journal of The Electrochemical Society*, 1997, **144**, 2045-2052.
12. X. W. Lou, Y. Wang, C. Yuan, J. Y. Lee and L. A. Archer, *Advanced Materials*, 2006, **18**, 2325-2329.
13. T. Gao, K. Huang, X. Qi, H. Li, L. Yang and J. Zhong, *Ceramics International*, 2014, **40**, 6891-6897.
14. J. Y. Huang, L. Zhong, C. M. Wang, J. P. Sullivan, W. Xu, L. Q. Zhang, S. X. Mao, N. S. Hudak, X. H. Liu, A. Subramanian, H. Fan, L. Qi, A. Kushima and J. Li, *Science*, 2010, **330**, 1515-1520.
15. M. Armand and J. M. Tarascon, *Nature*, 2008, **451**, 652-657.
16. Y.-M. Chiang, *Science*, 2010, **330**, 1485-1486.
17. J. N. Reimers and J. R. Dahn, *Journal of The Electrochemical Society*, 1992, **139**, 2091-2097.
18. The formation enthalpy is caculted on the data from HSC Chemistry 6
19. P. Poizot, S. Laruelle, S. Grugeon, L. Dupont and J. M. Tarascon, *Nature*, 2000, **407**, 496-499.

20. Q. Su, D. Xie, J. Zhang, G. Du and B. Xu, *ACS Nano*, 2013, **7**, 9115-9121.
21. L. Luo, J. Wu, J. Xu and V. P. Dravid, *ACS Nano*, 2014, **8**, 11560-11566.
22. K. E. Gregorczyk, Y. Liu, J. P. Sullivan and G. W. Rubloff, *ACS Nano*, 2013, **7**, 6354-6360.
23. J. Cabana, L. Monconduit, D. Larcher and M. R. Palacín, *Advanced Materials*, 2010, **22**, E170-E192.
24. P. Meduri, E. Clark, E. Dayalan, G. U. Sumanasekera and M. K. Sunkara, *Energy & Environmental Science*, 2011, **4**, 1695-1699.
25. P. Meduri, C. Pendyala, V. Kumar, G. U. Sumanasekera and M. K. Sunkara, *Nano Letters*, 2009, **9**, 612-616.
26. C. Wang, A. J. Appleby and F. E. Little, *Solid State Ionics*, 2002, **147**, 13-22.
27. C. Kim, M. Noh, M. Choi, J. Cho and B. Park, *Chemistry of Materials*, 2005, **17**, 3297-3301.
28. R. Ayouchi, F. Martin, J. R. Ramos Barrado, M. Martos, J. Morales and L. Sánchez, *Journal of Power Sources*, 2000, **87**, 106-111.
29. J. Xie, N. Imanishi, A. Hirano, Y. Takeda, O. Yamamoto, X. B. Zhao and G. S. Cao, *Solid State Ionics*, 2010, **181**, 1611-1615.
30. E. Fazio, F. Neri, S. Savasta, S. Spadaro and S. Trusso, *Physical Review B*, 2012, **85**, 195423.
31. S. H. Sun, G. W. Meng, G. X. Zhang, T. Gao, B. Y. Geng, L. D. Zhang and J. Zuo, *Chemical Physics Letters*, 2003, **376**, 103-107.
32. M. S. Sellers, A. J. Schultz, C. Basaran and D. A. Kofke, *Physical Review B*, 2010, **81**, 134111.
33. S.-M. Paek, E. Yoo and I. Honma, *Nano Letters*, 2008, **9**, 72-75.
34. M.-S. Park, G.-X. Wang, Y.-M. Kang, D. Wexler, S.-X. Dou and H.-K. Liu, *Angewandte Chemie*, 2007, **119**, 764-767.
35. S. Han, B. Jang, T. Kim, S. M. Oh and T. Hyeon, *Advanced Functional Materials*, 2005, **15**, 1845-1850.
36. S. Hy, F. Felix, J. Rick, W.-N. Su and B. J. Hwang, *Journal of the American Chemical Society*, 2014, **136**, 999-1007.